Journal Pre-proof

High-Resolution Topochemical Analysis and Thermochemical Simulations of Oxides and Nitrides at Grain Boundaries and within the Grains of a Low Alloy Mn-Cr Hot-rolled Steel Sheet

Vera G. PRAIG, Michael STÖGER-POLLACH, Arno SCHINTLMEISTER, Michael AUINGER, Herbert DANNINGER

This is a PDF file of an article that has undergone enhancements after acceptance, such as the addition of a cover page and metadata, and formatting for readability, but it is not yet the definitive version of record. This version will undergo additional copyediting, typesetting and review before it is published in its final form, but we are providing this version to give early visibility of the article. Please note that, during the production process, errors may be discovered which could affect the content, and all legal disclaimers that apply to the journal pertain.

High-Resolution Topochemical Analysis and Thermochemical Simulations of Oxides and Nitrides at Grain Boundaries and within the Grains of a Low Alloy Mn-Cr Hot-rolled Steel Sheet

Vera G. PRAIG[a,d], Michael STÖGER-POLLACH[a], Arno SCHINTLMEISTER[b], Michael AUINGER[a,c,d,*], Herbert DANNINGER[a,d,*]

[a]*Institute of Chemical Technologies and Analytics, Technische Universität Wien, Getreidemarkt 9, 1060 Vienna, Austria*
[b]*Large-Instrument Facility for Environmental and Isotope Mass Spectrometry, Centre for Microbiology and Environmental Systems Science, University of Vienna, 1090 Vienna, Austria*
[c]*WMG, University of Warwick, Coventry CV4 7AL, United Kingdom*
[d]*Christian Doppler Laboratory for Diffusion and Segregation Processes during the Production of High Strength Steel Sheet*

Abstract

The selective oxidation underneath the scale layer of an industrially hot rolled Fe-1.8Mn-0.8Cr steel at temperatures between 600-700°C has been investigated. The spatial distribution and composition of formed precipitates has been studied by high-resolution topochemical analysis via TEM-EELS and NanoSIMS and revealed heterogeneities in chemical composition, especially along grain boundaries. It could be shown that grain boundary oxides are predominantly composed of aluminium, chromium or silicon oxides/nitrides, surrounded by manganese-rich oxides. Experimental results of phase stability have been compared to numerical simulations, considering the distribution of more than 40 potentially stable oxide-, nitride- and carbide phases and differences are critically discussed.

Keywords: A. metals and alloys, C. grain boundaries, C. oxidation, D. atom, molecule, and ion impact (NanoSIMS), D. thermodynamic modelling

1. Introduction

Advanced high strength steels are very important for the automotive and construction materials sector. Due to their superior mechanical performance such as high tensile and yield strength combined with excellent ductility, they are often used for the safety structure in cars as well as for crash-sensitive parts [1]. Various steel grades are available such as dual phase steels (DP) [2], complex phase steels (CP) [3] or TRIP/TWIP-steels [4] which are each iron-based alloys contining ≈2 wt.% manganese and moderate amounts of either chromium, aluminium or silicon.

After (continuous) casting, these alloys are often hot rolled to sheet material with an optional hot forming stage to obtain the final shape of the workpiece. Especially during hot rolling and coil cooling, the material suffers considerably from oxidation [5], both externally and internally. Whereas the external oxides (termed "scale layer") can be removed rather easily, the formation of internal oxides both inside the grains (termed "bulk oxides" or "inner oxides") and along grain boundaries (termed "grain boundary oxides") lead to problems during subsequent pickling, cold forming and coating processes. Before strategies for mitigating the effect of internal oxides can be applied, the formation and composition of internal oxides [6, 7, 8, 9] needs to be understood further into detail, which has been the main scope of this study. Since these oxides are formed underneath the external scale layer [10], the local oxygen partial pressure is below the onset of wüstite formation ($\approx 5\times10^{-22}$ bar O_2 at 700 °C) but sufficiently high for selective oxidation of the added alloy elements. This oxidation not only lowers the concentrations of dissolved alloy elements and thus changes

---

the stability of phases [11], it also causes problems with crevice corrosion along grain boundaries in subsequent pickling [12, 13] and/or weakens cohesion between individual grains during subsequent forming processes. The removal of the oxide-affected zone thus requires additional post-treatment of hot formed steel grades, which increases both cost and loss of material [14].

Besides the wealth of information that can be found on the (grain boundary) oxide formation in such industrial steel grades [10, 11, 15, 16], the present work aims at more detailed investigation of the fine structure of formed grain boundary precipitates as well as the role of nitrides on the oxide formation and microstructure of grain boundary oxides and inner oxides. Accordingly, the present study focuses on a low/medium manganese dual phase (DP) steel grade from industrial production, as opposed to synthetic model alloys from lab exposures. This will account for the multitude of elements that ultimately define the precipitate microstructure. Our findings on the internal oxide and nitride formation, obtained from industrial steel grades under typical industrial hot rolling and coil cooling conditions, are compared to numerical simulations of element transport and thermodynamic stability of the formed phases. Consequently, the drawn conclusions can be applied more generally on steels and high temperature alloys. Furthermore, theoretical results can also be helpful to understand the formation and microstructure of high temperature corrosion products inside the metallic grains and along grain boundaries in boiler steels [17, 18], or for turbine blades [19, 20] and how the formation of precipitates can be affected by small amounts of nitride inclusions in the alloys.

2. Experimental Procedures

In order to obtain results representative for industrial production, an industrial steel grade (composition see table 1) was sampled directly after hot-rolling under production conditions and used for the lab-scale heat exposures. The topmost zone, which contained the formed scale layer as well as possible segregation of elements near the alloy/oxide interface, was removed mechanically by grinding and the samples were then polished with SiC grinding paper down to 2500 grit size. Obtained samples were then subjected to a heat treatment at temperatures between 600-700 °C for 1 h in dry air and then slowly cooled down to 550 °C over a period of 3.5 h, which is termed in this work as a "complete coil cooling cycle". After cooling down to room temperature, the heat-treated samples were cut into square shaped pieces of 15 mm × 15 mm × 2 mm in size using a diamond saw.

Table 1: Composition of an industrial Cr-Mn steel, provided by voestalpine Stahl GmbH. Concentrations were determined by atomic absorption spectrometry (AAS).

C (wt.%)	Al (wt.%)	Cr (wt.%)	Mn (wt.%)	Si (wt.%)	N (ppm wt.)	S (ppm wt.)	P (ppm wt.)	Fe
0.1	0.1	0.8	1.8	0.1	<50	<10	<200	bal.

Where necessary, the samples were mounted in epoxy resin (PolyFast, Struers) for further preparation. Normal cross sections (90°) for standard analysis were prepared as well as polished sections with a 25° tilt angle relative to the specimen surface in order to enlarge the depth of the oxidised zone by a factor of 2.37. All sections were mechanically ground by using grinding papers from 400 down to 2500 grit size and polished with 1 μm diamond paste. Prior to analysis, all samples were ultrasonically cleaned in ethanol and dried in a cold stream of dry air. On the samples intended for nanometer-scale secondary ion mass spectrometry (NanoSIMS), thin AuPd films were sputter-deposited to prevent electrical charging during the NanoSIMS measurement process The nominal coating thicknesses were 50 nm on the front side and 180 nm on the back side of the sample. NanoSIMS measurements were performed on a NS50L from Cameca (Genevilliers, France). Prior to data acquisition, analysis areas were pre-sputtered by scanning of a high-intensity, slightly defocused Cs^+ ion beam (spot size ca. 2 μm at 400 pA beam current) to remove the AuPd coating within the field of view and to establish the steady state signal intensity regime. In order to avoid crater edge effects, scanning during pre-sputtering was conducted over square-sized areas with an edge length exceeding the frame size of the subsequently recorded images by at least 15 μm. Imaging was conducted by sequential scanning of a finely focused Cs^+ primary ion beam (2 pA beam current) over areas ranging from 19 μm × 19 μm to 65 μ × 65 μm at a physical resolution of ca. 70 nm (probe size) and an image resolution of 512 × 512 pixels. Data were acquired as multilayer image stacks with a per-pixel dwell time of 10 ms per cycle. The total per-pixel dwell times ranged from 150 msec to 270 msec, corresponding to a total acquisition time of 11 h to 20 h per measurement. $^{12}C^-$, $^{16}O^-$, $^{12}C^{14}N^-$, $^{28}Si^-$, $^{31}P^-$ and $^{32}S^-$ as well as secondary electrons were simultaneously detected and the mass

spectrometer was tuned for achieving a mass resolving power of >8000 (according to Cameca's definition). Evaluation of the image data was carried out, using the WinImage software package (version 2.0.8) provided by Cameca. Prior to stack accumulation, the individual images were aligned to compensate for positional variations arising from primary ion beam and/or sample stage drift. Secondary ion signal intensities were corrected for detector dead-time on a per-pixel basis. Electron microscopy analysis comprised scanning electron microscopy (SEM, FEI Quanta 200 k, The Netherlands) and transmission electron microscopy / electron energy loss spectroscopy (TEM/EELS, FEI TECNAI 20, The Netherlands) at 20 nm lateral resolution [21]. SEM was applied on all sample cross sections, TEM/EELS was conducted on thin lamellae obtained by focused ion beam (FIB) sectioning of polished cross sections using a FIB FEI Quanta 300 2D dual beam equipped with a Ga liquid metal ion source (5-30 kV).

3. Mathematical Modelling

Numerical simulations of the internal oxidation process and local phase distributions were carried out by the subsequent two-step algorithm "ASTRID" [22], consisting of element migration and local thermodynamic equilibrium calculations. Transport of the atomic species (oxygen, nitrogen, iron and the alloying elements) has been derived from the system of partial differential equations. Diffusion coefficients are listed in table 2 and were chosen from literature. The considered thermodynamic phases are provided in table 3.

Table 2: Diffusion coefficients of alloy elements in ferrite.

Element	D^o / m^2 s^{-1}	E_a / kJ mol^{-1}	$D_{(700\,°C)} = D^o exp(\frac{E_a}{RT})$ / m^2 s^{-1}	Refs.
iron (Fe)	1.21×10^{-2}	281.6	9.27×10^{-18}	[23, 9]
oxygen (O)	3.72×10^{-6}	42.40	1.97×10^{-8}	[23, 9]
nitrogen (N)	7.80×10^{-7}	79.04	4.46×10^{-11}	[23, 24]
carbon (C)	3.94×10^{-7}	80.22	1.95×10^{-11}	[23, 14]
aluminium (Al)	1.8×10^{-4}	228.2	1.01×10^{-16}	[23, 9]
chromium (Cr)	8.52×10^{-4}	250.8	2.94×10^{-17}	[23, 9]
manganese (Mn)	7.60×10^{-5}	224.6	6.68×10^{-17}	[23, 9]
silicon (Si)	1.7×10^{-4}	229.1	8.57×10^{-17}	[23, 9]

Table 3: Stable thermodynamic phases for the simulations, based on the FactSage Steel database (FSstel).

Fe, C, O$_2$, N$_2$	Al	Cr	Mn	Si
FeO, Fe$_3$O$_4$	Al$_2$O$_3$	Cr$_2$O$_3$	MnO, Mn$_3$O$_4$	SiO$_2$
Fe$_4$N	AlN	CrN, Cr$_2$N	Mn$_4$N, Mn$_6$N$_4$, Mn$_6$N$_5$	Si$_3$N$_4$
	Al$_4$C$_3$	Cr$_{23}$C$_6$, Cr$_7$C$_3$, Cr$_3$C$_2$	Mn$_3$C, Mn$_5$C$_3$, Mn$_7$C$_3$, Mn$_{23}$C$_6$	SiC
FeAl$_2$O$_4$, FeSiO$_3$, Fe$_2$SiO$_4$, FeCr$_2$O$_4$, MnFe$_2$O$_4$, Al$_2$SiO$_5$, MnAl$_2$O$_4$, MnSiO$_3$, Mn$_2$SiO$_4$				
Si$_2$ON$_2$				

The temperature program comprised of an isothermal holding at 700 °C for 1 h and subsequent slow, linear cooling down to 550 °C over a period of 3.5 h. As stated above, in the present work this is termed as a "complete coil cooling cycle". Since the industrial steel grade appears to be mostly ferritic at process temperatures (see figure B.8 in the appendix), the ferrite phase specific diffusion properties were considered. The alloy content of the samples in this study was either too low to stabilise the austenite phase or did not stabilise the austenite phase at all. Hence, depletion of dissolved alloy element additions (C, Al, Cr, Mn, Si) due to oxide formation does not lead to a phase change in the experiments.

The oxygen concentration at the surface (upper boundary) was set to a constant value, according to the maximum solubility of oxygen for the iron/wüstite equilibrium at the applied temperatures (0.45 ppm [O] at 700 °C, see [25]) which corresponds to a scenario of maximum internal oxidation underneath the external scale layer. This corresponds to the constant source model firstly proposed by Wagner [26], which applies to the actual conditions at the iron/wüstite interface with sufficient accuracy. Accordingly, this assumption is most commonly used in theoretical simulation

studies on internal oxidation [9, 14, 10, 27, 28, 29]. Since the external scales of our industrial samples contained a large number of cracks, maximum nitrogen uptake was assumed as well [24, 30]. Hence the nitrogen concentration at the surface (upper boundary) was set to a constant value which corresponds to the solubility of nitrogen at 1 bar (25.0 ppm [N] at 700 °C, see [31]). The calculation of elemental transport via diffusion has been carried out for small time intervals ($\leqslant$1 min). The results after each calculation step were used to derive the local concentrations of each phase with the thermodynamic subroutine ChemApp (GTT-Technologies, Germany) [32]. The amount of each phase obtained from the equilibrium calculation was set as the starting value for the diffusion calculation in the next time interval. After the final simulation step, the results were displayed similar to a line scan along the specimen's cross section, indicating the relative amount and spatial distribution of each stable phase. Since the large number of considered thermodynamic phases (see table 3) and the complex sample microstructure necessitate a large number of input parameters, it was decided to exclude the effect of grain boundaries from the computations. Adding this influence would have further increased the number of input parameters and the uncertainty of computed results. Due to this and for reasons of mathematical simplicity - a complex microstructure also causes longer simulation times - it was decided that this theoretical approach represents a good compromise for evaluation of experimental observations. As a consequence, thermodynamic phases containing phosphorus or sulphur were excluded from the simulations. Both elements are known to segregate strongly at grain boundaries but the low nominal concentrations in the alloy would have a minor effect on modelled phase distributions.

The main groups of precipitates (oxides, nitrides and carbides) are highlighted in the presented results. Correspondingly, concentrations of aluminium, chromium, manganese and silicon within these precipitates are displayed. This mode of presentation has been chosen to facilitate identification of the interactions between oxygen, nitrogen and carbon during heat exposure.

4. Results and Discussion

Industrial steel grades, as opposed to perfectly homogeneous binary and ternary model alloys, contain a multitude of elements and are prone to small variations in local composition. Thus, results from a single measurement may not be representative for the behaviour of the entire alloy which is why several replicate analyses were conducted and the discussion focuses on the most common observations.

Numerical simulations of the spatial distribution of stable phases reveal three distinct regions of thermodynamically stable precipitates (*oxides - nitrides - carbides*), as shown in figure 1. After the heat treatment, a 5-6 μm wide zone of internal oxides has emerged beneath the surface. According to the chemical composition, the most dominant precipitates are thermodynamically stable spinel-type oxides ($M^{+II}M_2^{+III}O_4$), followed by other mixed and pure alloy element oxides. This domain is followed by a 40 μm wide zone containing nitride precipitates. During the high temperature treatment, the zone of nitrides gradually moves inwards as the oxidation proceeds. This so-called "push-effect" [33] on the macroscopic scale in fact relies on a substitution of nitrogen atoms in the existing precipitates by oxygen, since oxides are thermodynamically more stable than the corresponding nitride phases (see figure B.8). A narrow region of silicon-oxynitrides is visible between the oxide and nitride zones, which is consistent with the thermodynamic predictions. It should be noted that the local nitrogen activity in-between the oxide/nitride zones reaches values close to the partial pressure of nitrogen in the gas atmosphere ($\approx$1 bar) since there are no stable nitrides within the oxide zone but only diffusion of dissolved nitrogen. In this context, it should further be noted that transformation of aluminium nitrides into oxides at $p(N_2)$ = 1 bar necessitates an oxygen partial pressure of 10^{-33} bar. Such an oxygen partial pressure is remarkably close to the onset of oxide formation for manganese and, to some extent, also for chromium (figure B.8). This is also indicated by the slight overlap in the computed oxide and nitride phase distributions in figure 1. Very little evidence was found on the miscibility of nitrides in literature [34, 35, 36]. Hence, the formed nitrides will indeed separate the alloy elements whereas oxides can thermodynamically form mixed spinel phases - if not already spatially separated by previous nitride formation.

The bulk of the alloy contains carbides, which are stable at more than 45 μm beneath the alloy surface. Again, a "push-effect", mimicking migration of carbides by nitrides, is indicated. However, in contrast to the above described transformation of nitrides into oxides, the released carbon is enriched underneath the nitride zone which manifests itself in an increase of the carbide content directly underneath the nitride zone. This behaviour is well known and very common during nitride hardening processes [33, 37]. In extreme cases, the local activity of carbon reaches values by which a small peak of dissolved carbon in the iron matrix can be observed (see the region of dissolved carbon in

figure 1). This fraction of mobile carbon diffuses towards the bulk of the sample and forms the sudden hump in the carbide profile at around 48 μm below the surface.
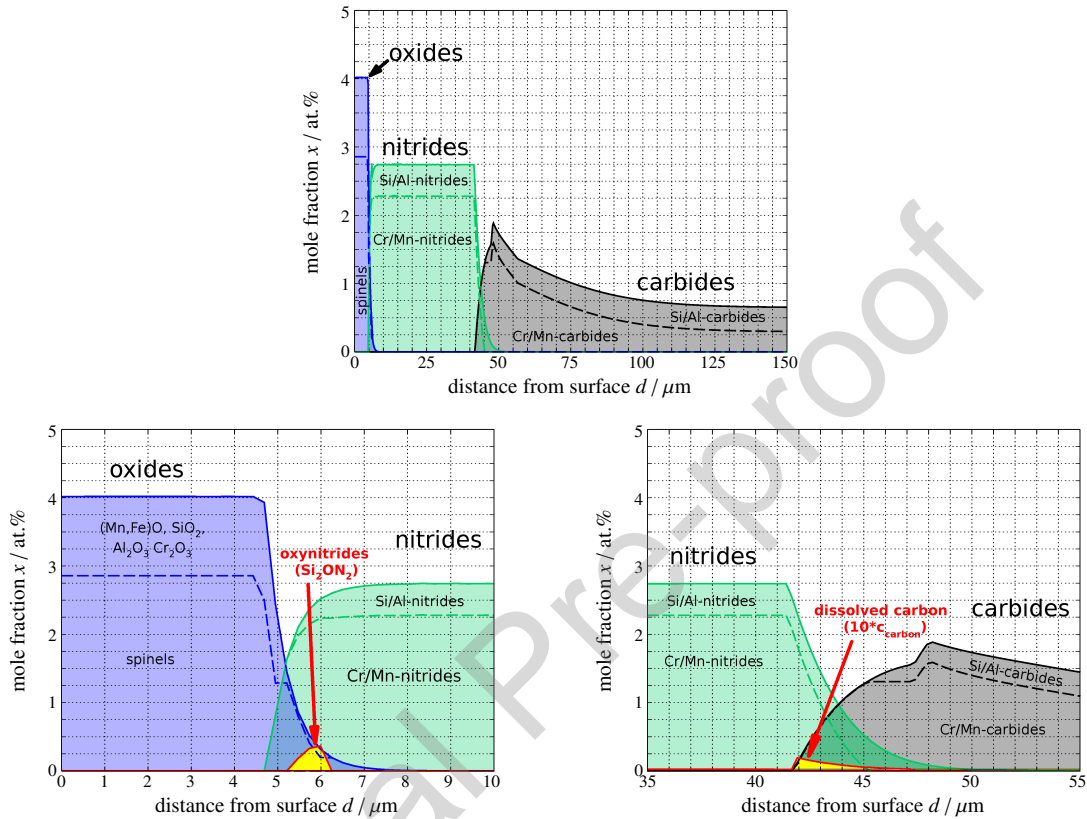

Figure 1: Simulation results of oxide/nitride/carbide distributions in an industrial grade Fe-1.8Mn-0.8Cr steel after a complete coil cooling cycle (top). Detail of oxide/nitride boundary zone, showing the presence of oxynitrides (bottom left) and nitride/carbide boundary zone, showing the presence of mobile carbon (bottom right). Note that the concentration of carbon dissolved in the ferrite phase (dissolved carbon) has been multiplied by 10 to enhance visibility.

The simulation results for the depth of the bulk oxide zone (5-6 μm) agree fairly well with experimental results from figure 2 (1-3 μm). A pronounced oxidation along grain boundaries can be observed, which matches with the formation of silicon-rich oxides. The distributions of Mn, Cr and Al were not measured due to limited NanoSIMS measurement time and the interested reader is referred to another publication that discusses the oxidation behaviour in ternary model alloys [9]. Although it has been shown in previous studies that the oxidation along grain boundaries follows tabulated diffusion values, it should be noted that diffusion coefficients along grain boundaries are 100-1000 times larger than bulk diffusion coefficients which have been used for the simulations in figure 1. In the same work [9] it is also mentioned that for internal oxidation, the bulk diffusion of oxygen is slowed down, which explains the lower bulk oxidation depth of $\approx 2\,\mu$m in figure 2 as compared to the 5-6 μm wide zone in the simulations of figure 1.

A clear difference between simulations and experiment can be seen for the existence of the nitride zone, which is absent in the experimental data. This discrepancy is caused by the formation of an external scale during the industrial processing. This (oxide) scale layer is known to inhibit transport of nitrogen from the gas phase into the material [17]. In contrast to this, a maximum uptake of nitrogen from the gas atmosphere was assumed in the simulations, depending on the nitrogen partial pressure. Albeit only indicative, it should be noted that the concentration of nitrogen in the zone of oxides appears to be slightly lower than deeper inside the material. Here, the nitrides seem to have mixed with carbides that emerge below the oxidised zone. Larger precipitates can be observed in this area, and the lamellar structure of the carbon distribution within individual grains indicate the presence of pearlite [38] in the alloy.

A strong segregation of sulphur and phosphorus at grain boundaries has also become evident from the NanoSIMS measurements (figure 2).
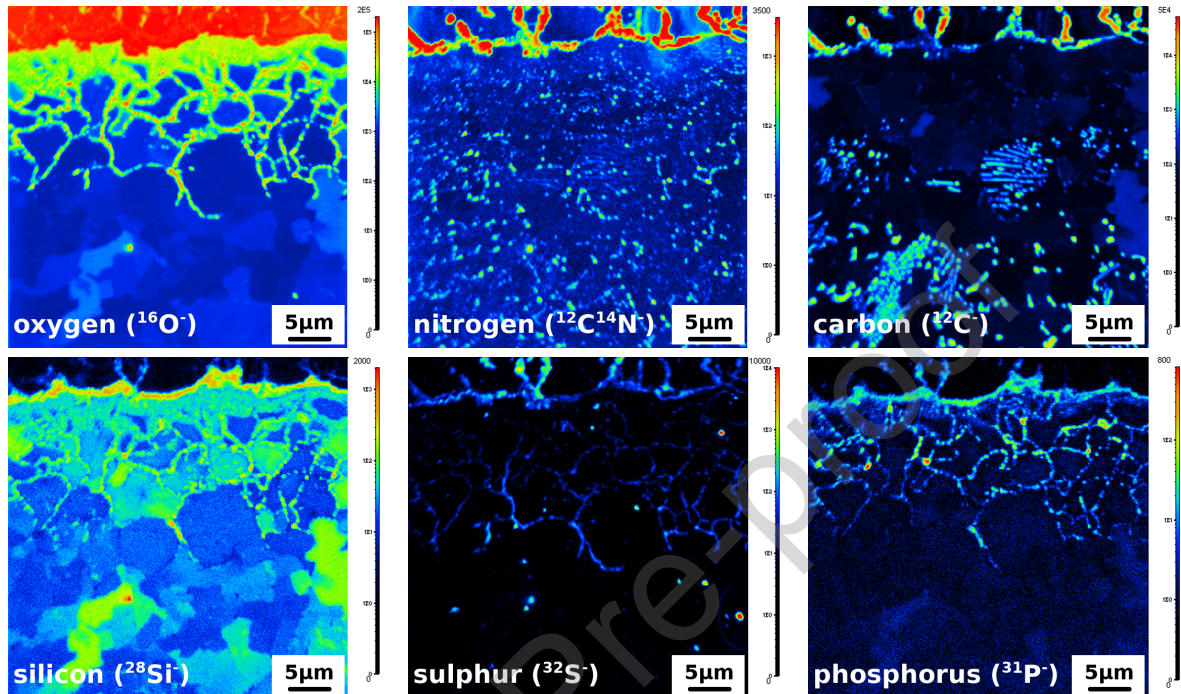

Figure 2: NanoSIMS secondary ion signal intensity distribution images of selected elements in an industrial grade Fe-1.8Mn-0.8Cr steel after a complete coil cooling cycle of 4.5h. The scale/metal interface of the steel sample is located close to the top edge of the images. Polished cross sections were prepared with a 25° tilt angle, to enlarge the vertical view of the oxidised zone by a factor of 2.37. Signal intensities, given in counts per second, are displayed on a logarithmic false-color scale, ranging from dark blue to red for low to high intensities, respectively.

Detailed scans of the oxide-affected zone are shown in figure 3, which reveal the difference between inner oxides and grain boundary oxides. The concentration of sulphur and phosphorus along grain boundaries is lower in close proximity to the surface, which indicates that both elements also suffer from a "push-effect" due to oxide formation (e.g. transformation of MnS to MnO [18]) because the concentration of sulphur and phosphorus clearly reaches a maximum near the internal oxidation front. This observation qualitatively underpins the assumption from literature that sulphur and phosphorus are pushed inwards as the front of oxides/nitrides and carbides grows, since the concentration of sulphur and phosphorus suddenly drops towards the center of the alloy.

TEM images of heat-treated samples (figure 4) reveal a fine dispersion of 50-100 nm sized precipitates near the internal corrosion front. As can be seen from the corresponding elemental scans, both nitrides and oxides have been formed. Here, the distribution of oxides and nitrides is not homogeneous but instead a distinct peak of nitrides is exhibited in the center of the grain boundary domain (*i*). According to the higher thermodynamic stability of oxides relative to nitrides (see figure A.7 in the appendix), this nitride peak could be explained by the partial substitution of nitrogen by oxygen during oxidation. Consequently, bound nitrogen is released into the material [24, 30] or pushed to the center of the grain boundary precipitate where the nitrogen activity exceeds the critical limit to stabilise the nitride phase. According to the elemental scans of manganese and chromium in figure 4, it is likely that the center of this particular grain boundary is composed of manganese/iron-rich nitrides. Since the concentration of aluminium and silicon was below the limit of detection in this measurement, their presence in minor amounts, however, cannot be safely excluded in these nitrides as well.

In contrast to many literature sources [10, 6, 5, 39, 40], which assume the presence of the thermodynamically most stable spinel $(Fe_{1-x-y}Mn_xCr_y)_3O_4$ for internal oxidation of manganese-chromium steels, the distribution of chromium and manganese in figure 4 shows a small overlap of both elements, indicating the presence of binary Mn and Cr
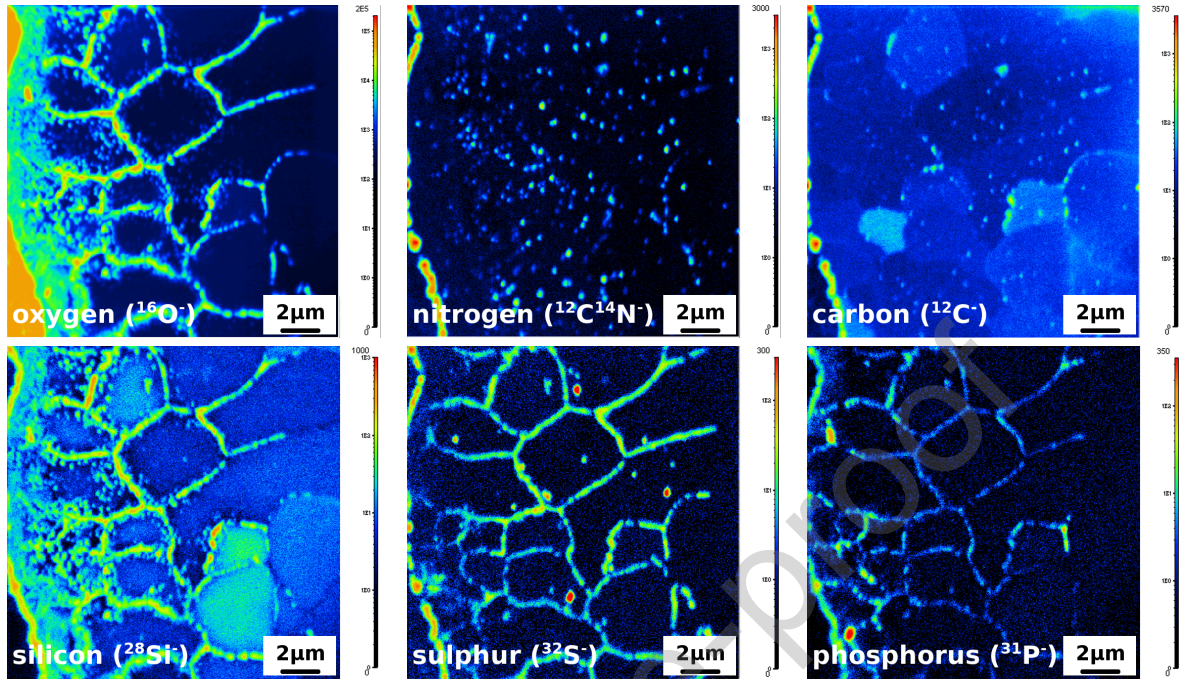
Figure 3: Detailed NanoSIMS secondary ion signal intensity distribution images of selected elements in the near-surface region of in an industrial grade Fe-1.8Mn-0.8Cr steel after a complete coil cooling cycle of 4.5h. The scale/metal interface of the steel sample is located close to the left edge of the images. Cross sections were prepared with a regular 90° angle. Signal intensities, given in counts per second, are displayed on a logarithmic false-color scale, ranging from dark blue to red for low to high intensities, respectively.

oxides, respectively. It is unlikely that this separation was caused by a decomposition of the spinel phase during cooling from 700 °C down to room temperature. The resulting Cr_2O_3 and $(Fe_{1-x}Mn_x)O$ would still be more evenly distributed throughout the internal oxides [18, 9, 39].
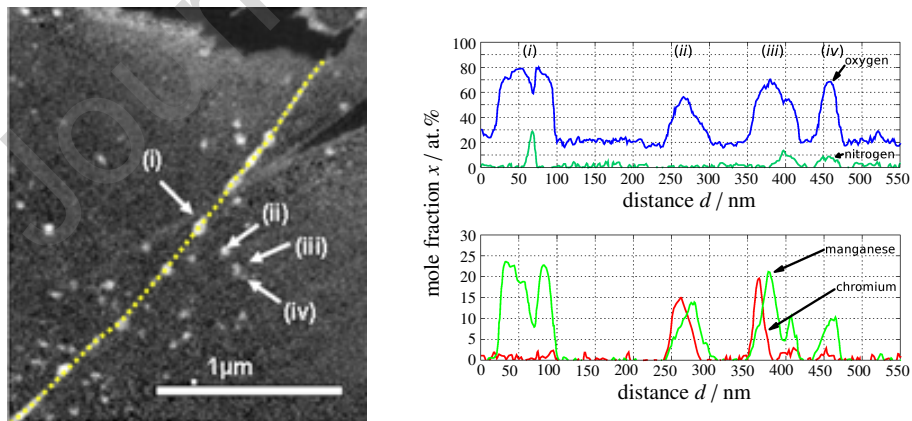

Figure 4: TEM-image (left) and EELS profile (right) of a grain boundary oxide (*i*) and internal oxides (*ii-iv*) in a hot-rolled Fe-1.8Mn-0.8Cr industrial-grade steel sheet after the completed coil cooling programme. The direction of the grain boundary is indicated by the dashed line in the left TEM-image and located close to the internal corrosion front.

Two-dimensional elemental maps of another grain boundary close to the internal corrosion front (see figure 5) confirm the separation of manganese and chromium. Here, the center of the grain boundary is composed of chromium-

7

rich oxides which again show a small overlap with the surrounding manganese oxides. Small amounts of nitrides were detected in the center of the grain boundary oxide and at the outer periphery of the manganese-rich oxides. The higher thermodynamic stability of oxides (see figure A.7) suggests that oxygen diffused along grain boundaries and substituted nitrogen in the formed precipitates. Arguably, the continuous band of chromium oxides along the original grain boundary might indicate that this phase was formed first. However, since the equilibrium conditions of manganese and chromium oxide/nitride formation are very similar in this alloy, the initial formation of chromium may have simply been caused by lattice misfits that affect nucleation and growth of formed oxidation products [10, 41, 42, 43].
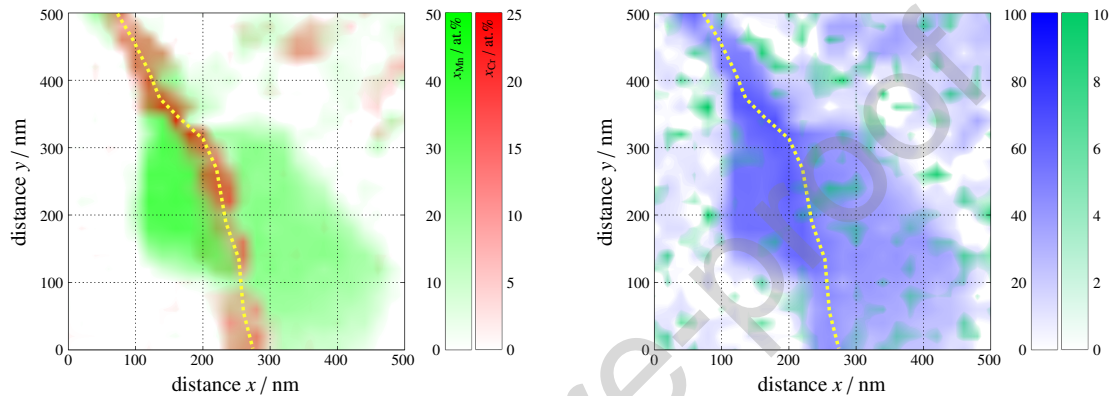

Figure 5: TEM-EELS elemental maps of (left) manganese (green), chromium (red) and (right) oxygen (blue), nitrogen (green) near the grain boundary of a hot rolled Fe-1.8Mn-0.8Cr industrial grade steel sheet after the completed cooling programme. Note the marginal overlap of the elements in both images. The dashed yellow line in both graphs indicates a string of chromium-rich oxides and the direction of the original grain boundary close to the internal corrosion front. These chromium-rich oxides are thermodynamically stable but may originate from pre-existing nitride and/or carbide precipitates that formed first during heat exposure.

Remarkably, the results from figures 4 & 5 give rise to the hypothesis that transport properties along oxidised grain boundaries are varying. Whereas the vast majority of available literature assumes the properties of grain boundaries to be homogeneous (due to lack of detailed data), the observed spatial oxide/nitride distributions clearly indicate that element transport attains another level of complexity that is beyond the reported values and texture dependence of grain boundary diffusion coefficients for high temperature corrosion simulations [10, 23]. Oxygen transport along grain boundaries may thus not occur through the entire grain boundary, as proposed by the classical diffusion models of Wagner [26] and Fisher [44, 45] but preferentially takes place at the oxide/metal interface. Interfaces and grain boundaries are often the origin for fast transport in ionic crystals [46, 16, 47]. As a consequence, the diffusion model by Wagner and Fisher may need to be refined such that the grain boundary domain is further separated into "interface" and "bulk oxide" regions. Although this would theoretically explain why nitrogen has been found in the center of grain boundary precipitates, it should be noted that a definite conclusion on the oxygen transport mechanism along grain boundaries cannot be drawn purely from the obtained results.

The separation of manganese, aluminium and silicon in internal oxides follows similar trends as observed for grain boundaries (figure 6). Due to the smaller size of the inner oxides (20 nm) and hence shorter diffusion paths, the separation of the alloy elements is smaller than within grain boundary oxides (90 nm). The center of the grain boundary in figure 6 contains a high amount of aluminium, which has a high affinity to both nitrogen and oxygen (figure A.7). It is thus assumed that this phase was formed first. Again, according to predominance diagrams (figure B.8), an oxygen partial pressure $p(O_2) = 10^{-33}$ bar is required for transformation of AlN into Al_2O_3 at 700 °C and a nitrogen partial pressure of 1 bar. This value matches almost exactly with the oxygen partial pressure of the Mn/MnO and Cr/Cr_2O_3 equilibria. For the upper limit of the oxygen partial pressure ($p(O_2) = 10^{-22}$ bar) defined by the iron/wustite equilibrium at the alloy/oxide scale interface, the calculated nitrogen partial pressure to stabilise aluminium nitrides is much higher than $p(N_2) = 10^{+5}$ bar. This means that based on bulk thermodynamic principles, no nitride phases are expected to be stable near the surface because the thermodynamic nitrogen partial pressure required would be far too

high. However, closer to the internal oxidation front, the presence and/or absence of sufficient amounts of manganese and chromium will indeed affect the transformation of nitrides into oxides and hence the structure of the formed grain boundary precipitates.
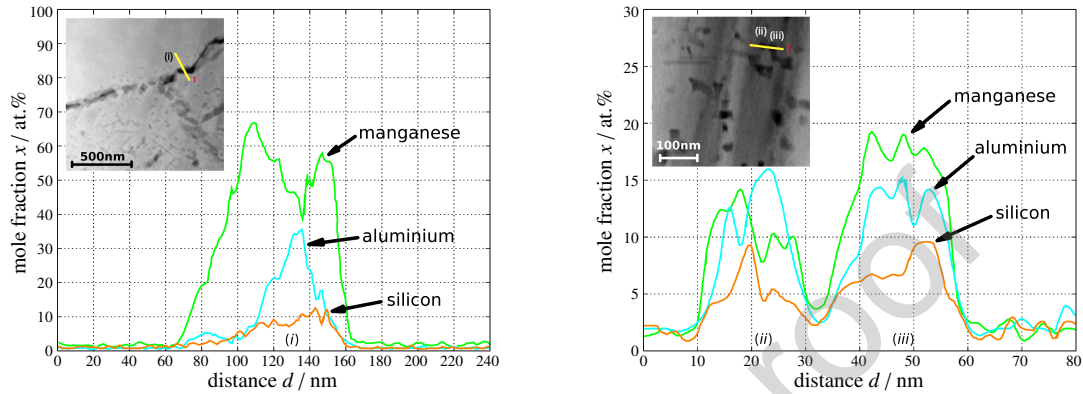

Figure 6: Relative concentration profiles of the alloy elements manganese, aluminium and silicon across a grain boundary oxide (*i*, left) and two closely adjacent internal oxides (*ii*, *iii*, right) of a hot-rolled Fe-1.8Mn-0.8Cr industrial-grade steel sheet after the completed coil cooling programme. The direction of the line scan is indicated by the yellow line in the TEM-images at the upper left corners and the position of the scans is close to the internal corrosion front.

5. Conclusions

High temperature oxidation studies and numerical simulations of phase stabilities for an industrial low-alloy Mn-Cr steel have been carried out. Numerical simulations of spatial phase distributions, in which more than 40 thermodynamic phases were considered, show three clearly separated zones from the surface to the core containing oxide, nitride and carbide precipitates in the alloy. The values of the oxidation depth agree reasonably well between theoretical predictions and experimental observations but deviate for the amount of formed nitrides. This deviation originates from the presence of an external wüstite scale at process temperatures, which serves as an oxygen reservoir for selective oxidation but blocks further nitrogen uptake from the reaction gas.

High resolution images of internal precipitates clearly show heterogeneities in their chemical composition instead of a homogeneous spinel-type oxide. Grain boundary oxides often seem to be composed of a layered structure with chromium, aluminium and nitrogen in the center, surrounded by manganese-rich oxides. This layered structure has not been reported before and is likely caused by distinct thermodynamic stabilities of the oxides which show similar oxygen activity values for manganese and chromium as well as for aluminium and silicon. However, the thermodynamically most stable spinel phases which are often speculated to be present at grain boundaries, are only observed in minor amounts. This is potentially due to the initial formation of immiscible alloy element nitrides which are eventually transformed into oxides. This fine-structure of oxides along grain boundaries may be an indication that oxygen transport is not uniform across the entire grain boundary domain as proposed by Fisher.

Whereas the same spatial separation between alloy elements exists for inner oxides as well, it appears to be much weaker compared to oxidation products formed along grain boundaries.

In addition to the detailed analyses of oxygen, nitrogen, carbon and the alloy elements, it could also be shown that a strong segregation of sulphur and phosphorus exists along the grain boundaries near the internal oxidation front.

Finally, it should be noted that the experimental investigations in this study were carried out on an industrial-grade steel. In contrast to perfectly homogeneous binary and ternary model alloys, industrial alloys contain a multitude of elements and are prone to small variations in local composition. Accordingly, several replicate analyses have been carried out and discussions have focussed on the most common observations. Future efforts are suggested to consider and characterize the microstructure of formed precipitates in model alloys more into detail.

9

6. Acknowledgements

References

[1] J. Rowe, Advanced materials in automotive engineering, 1st Edition, Woodhead Publishing, 2012.

[2] R. Davies, Influence of Martensite Composition Content on the Properties of Dual Phase Steels, Metallurgical Transactions A 9 (1978) 671–679.

[3] H. Leitner, M. Bischof, H. Clemens, S. Erlach, B. Sonderegger, E. Kozeschnik, J. Svoboda, F. Fischer, Precipitation Behaviour of a Complex Steel, Advanced Engineering Materials 8 (2006) 1066–1077.

[4] O. Grässel, L. Krüger, G. Frommeyer, L. Meyer, High strength Fe-Mn-(Al, Si) TRIP/TWIP steels development - properties - application, International Journal of Plasticity 16 (2000) 1391–1409.

[5] N. Birks, G. Meier, F. Pettit, High-Temperature Oxidation of Metals, 1st Edition, Cambridge University Press, Cambridge, 2006.

[6] P. Kofstad, High Temperature Corrosion, 1st Edition, Elsevier Applied Science, London, 1988.

[7] K. Kruska, S. Lozano-Perez, D. Saxey, T. Terachi, T. Yamada, G. Smith, Nanoscale characterisation of grain boundary oxidation in cold-worked stainless steels, Corrosion Science 63 (2012) 225–233.

[8] A. Fontaine, H. Yen, P. Felfer, S. Ringer, J. Cairney, Atom probe study of chromium oxide spinels formed during intergranular corrosion, Scripta Materialia 99 (2015) 1–4.

[9] M. Auinger, V. Praig, B. Linder, H. Danninger, Grain boundary oxidation in iron-based alloys, investigated by ^{18}O enriched water vapour - The effect of mixed oxides in binary and ternary Fe-{Al, Cr, Mn, Si} systems, Corrosion Science 96 (2015) 133–143.

[10] D. Young, High Temperature Oxidation and Corrosion of Metals, 1st Edition, Elsevier, Amsterdam, 2008.

[11] L. Liu, Z. Yang, C. Zhang, M. Ueda, K. Kawamura, T. Maruyama, Effect of water vapour on the oxidation of Fe-13Cr-5Ni martensitic alloy at 973 K, Corrosion Science 60 (2012) 90–97.

[12] J. Galvele, Transport Processes and the Mechanism of Pitting of Metals, Journal of the Electrochemical Society 123 (1976) 464–474.

[13] H. Schmidtbauer, P. Blaha, H. Danninger, B. Mayr-Schmölzer, DFT study on the adsorption mechanism of 2-butyne-1,4-diol on the Fe(100) surface as a corrosion inhibitor for steel pickling, Tech. rep., Vienna University of Technology (2015).

[14] M. Auinger, A. Vogel, D. Vogel, M. Rohwerder, Early stages of oxidation observed by in-situ thermogravimetry in low pressure atmospheres, Corrosion Science 86 (2014) 183–188.

[15] E. Essuman, G. Meier, J. Żurek, M. Hänsel, L. Singheiser, W. Quadakkers, Enhanced internal oxidation as trigger for breakaway oxidation of Fe-Cr alloys in gases containing water vapor, Scripta Materialia 57 (2007) 845–848.

[16] A. Heuer, T. Nakagawa, M. Azar, D. Hovis, J. Smialek, B. Gleeson, N. Hine, H. Guhl, H. Lee, P. Tangney, W. Foulkes, M. Finnis, On the growth of Al_2O_3 scales, Acta Materialia 61 (2013) 6670–6683.

[17] J. Zurek, G. Meier, E. Wessel, L. Singheiser, W. Quadakkers, Temperature and gas composition dependence of internal oxidation kinetics of an Fe-10%Cr alloy in water vapour containing environments, Materials and Corrosion 62 (2011) 504–513.

[18] V. Praig, M. Stöger-Pollach, Metallography of Low Alloy Cr-Mn Hot-Rolled Steel and Quantitative Evaluation of Grain Boundary- and Internal Oxides by TEM, Materials Science Forum 782 (2014) 284–287.

[19] F. Stott, G. Wood, D. Whittle, B. Bastow, Y. Shida, A. Villafane, The Transport of Oxygen to the Advancing Internal Oxide Front During Internal Oxidation of Nickel-Base Alloys at High Temperature, Solid State Ionics 12 (1984) 365–374.

[20] M. Bensch, A. Sato, N. Warnken, E. Affeldt, R. Reed, U. Glatzel, Modelling of High Temperature Oxidation of Alumina-Forming Single-Crystal Nickel-Base Superalloys, Acta Materialia 60 (2012) 5468–5480.

[21] M. Stöger-Pollach, Low voltage TEM: Influences on electron energy loss spectrometry experiments, Micron 41 (2010) 577–584.

[22] M. Auinger, R. Naraparaju, H. Christ, M. Rohwerder, Modelling High Temperature Oxidation in Iron-Chromium Systems: Combined Kinetic and Thermodynamic Calculation of the Long-Term Behaviour and Experimental Verification, Oxidation of Metals 76 (2011) 247–258.

[23] H. Mehrer, Landolt Börnstein - Numerical Data and Functional Relationships in Science and Technology, Group III: Condensed Matter, Vol. 26, Springer, 1990, Ch. Diffusion in Solid Metals and Alloys, pp. 1–744.

[24] M. Auinger, E. Müller-Lorenz, M. Rohwerder, Modelling and experiment of selective oxidation and nitridation of binary model alloys at 700 °C - The systems Fe, 1 wt.%{Al, Cr, Mn, Si}, Corrosion Science 90 (2015) 503–510.

[25] J. Swisher, E. Turkdogan, Solubility, Permeability, and Diffusivity of Oxygen in Solid Iron, Transactions of the Metallurgical Society of AIME 239 (1967) 426–431.

[26] C. Wagner, Theoretical Analysis of the Diffusion Processes Determining the Oxidation Rate of Alloys, Journal of the Electrochemical Society 99 (1952) 369–380.

[27] T. Nijdam, L. Jeurgens, W. Sloof, Modelling the thermal oxidation of ternary alloys-compositional changes in the alloy and the development of oxide phases, Acta Materialia 51 (2003) 5295–5307.

[28] W. Pragnell, H. Evans, A finite-difference model to predict 2D depletion profiles arising from high temperature oxidation of alloys, Modelling and Simulation in Materials Science and Engineering 14 (2006) 733–740.

[29] L. Bataillou, C. Desgranges, L. Martinelli, D. Monceau, Modelling of the effect of grain boundary diffusion on the oxidation of Ni-Cr alloys at high temperature, Corrosion Science 136 (2018) 148–160.

[30] J. Bott, H. Yin, S. Sridhar, M. Auinger, Theoretical and experimental analysis of selective oxide and nitride formation in Fe-Al alloys, Corrosion Science 91 (2015) 37–45.

[31] H. Zitter, L. Habel, On the solubility of nitrogen in pure iron and in austenitic chromium-nickel-steels, Archiv Eisenhüttenwesen 44 (1973) 181–188.

[32] S. Petersen, K. Hack, The thermochemistry library ChemApp and its Applications, International Journal of Materials Research 98 (2007) 935–945.

[33] M. Tsujikawa, N. Yamauchi, N. Ueda, T. Sone, Y. Hirose, Behavior of carbon in low temperature plasma nitriding layer of austenitic stainless steel, Surface & Coatings Technology 193 (2005) 309–313.

[34] T. Ekström, M. Nygren, SiAlON Ceramics, Journal of the American Ceramic Society 75 (1992) 259–276.

[35] E. Mittemeijer, ASM Handbook - Steel Heat Treating Fundamentals and Processes, Vol. 4A, J. Dossett AND G.E. Totten, 2013, Ch. Fundamentals of Nitriding and Nitrocarburizing, pp. 619–646.

[36] P. Wiggen, H. Rozendaal, E. Mittemeijer, The nitriding behaviour of iron-chromium-carbon alloys, Journal of Materials Science 20 (1985) 4561–4582.

[37] M. Auinger, M. Rohwerder, Coupling diffusion and thermodynamics - exemplified for the gas nitriding of iron-chromium alloys, HTM J. Heat Treatm. Mat. 66 (2011) 100–102.

[38] B. Bramfitt, A. Benscoter, https://books.google.co.uk/books?id=hoM8VJHTt24CMetallographer's Guide: Practice and Procedures for Irons and Steels, EngineeringPro collection, ASM International, 2001.
https://books.google.co.uk/books?id=hoM8VJHTt24C

[39] A. Marasco, D. Young, The Oxidation of Iron-Chromium-Manganese Alloys at 900°C, Oxidation of Metals 157-174 (1991) 36.

[40] Y. Li, J. Morral, A local equilibrium model for internal oxidation, Acta Materialia 50 (2002) 3683–3691.

[41] C. Wagner, Internal Oxidation of Cu-Pd and Cu-Pt Alloys, Corrosion Science 8 (1968) 889–893.

[42] D. Young, M. Burg, P. Munroe, Internal Precipitation of Al_2O_3 and Cr_2O_3 in Austenitic Alloys, Materials Science Forum 461-464 (2004) 21–28.

[43] R. Bosch, F. Lenel, G. Ansell, The influence of the rate of oxidation upon the properties of internally oxidized silver-magnesium alloys, Transactions of the ASM 57 (1964) 960–971.

[44] J. Fisher, Calculation of Diffusion Penetration Curves for Surface and Grain Boundary Diffusion, Journal of Applied Physics 22 (1) (1951) 74–77.

[45] G. Young, R. Funderlic, On the grain boundary diffusion theory of Fisher and Whipple, Journal of Applied Physics 44 (1973) 5151–5153.

[46] T. Frömling, H. Hutter, J. Fleig, Oxide Ion Transport in Donor-Doped $Pb(Zr_xTi_{1-x})O_3$: Near-Surface Diffusion Properties, Journal of the American Ceramic Society 95 (2012) 1692–1700.

[47] S. Hallström, L. Höglund, J. Ågren, Modeling of iron diffusion in the iron oxides magnetite and hematite with variable stoichiometry, Acta Materialia 59 (2011) 53–60.

[48] C. Bale, E. Bélisle, P. Chartrand, S. Decterov, G. Eriksson, K. Hack, I. Jung, Y. Kang, J. Melancon, A. Pelton, C. Robelin, S. Petersen, FactSage thermochemical software and databases - recent developments, CALPHAD 33 (2009) 295–311.

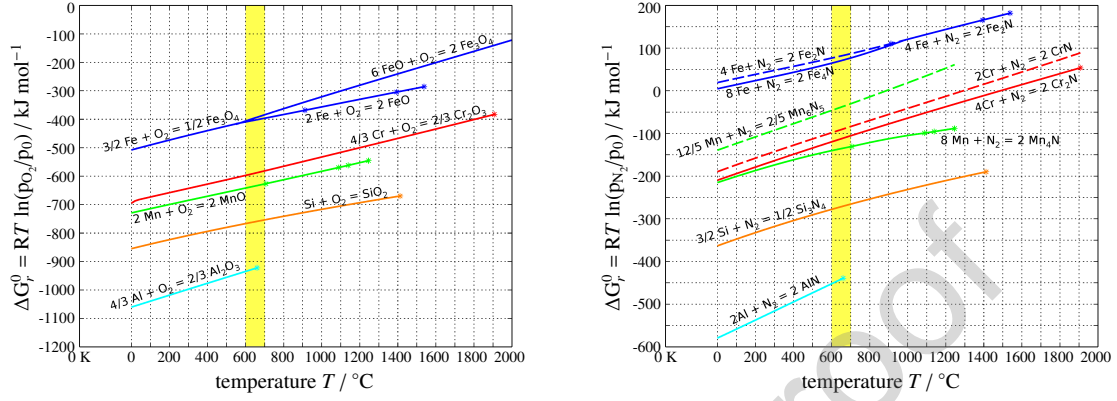# Appendix A. Phase Stability Diagrams

Figure A.7: Ellingham-Richardson diagrams of oxide (left) and nitride stability (right) of pure elements. The diagrams have been calculated with the FactSage Steels database (FSstel [48, 32]). Process temperature ranges for the heat exposure of industrial alloys in this study are highlighted in yellow.
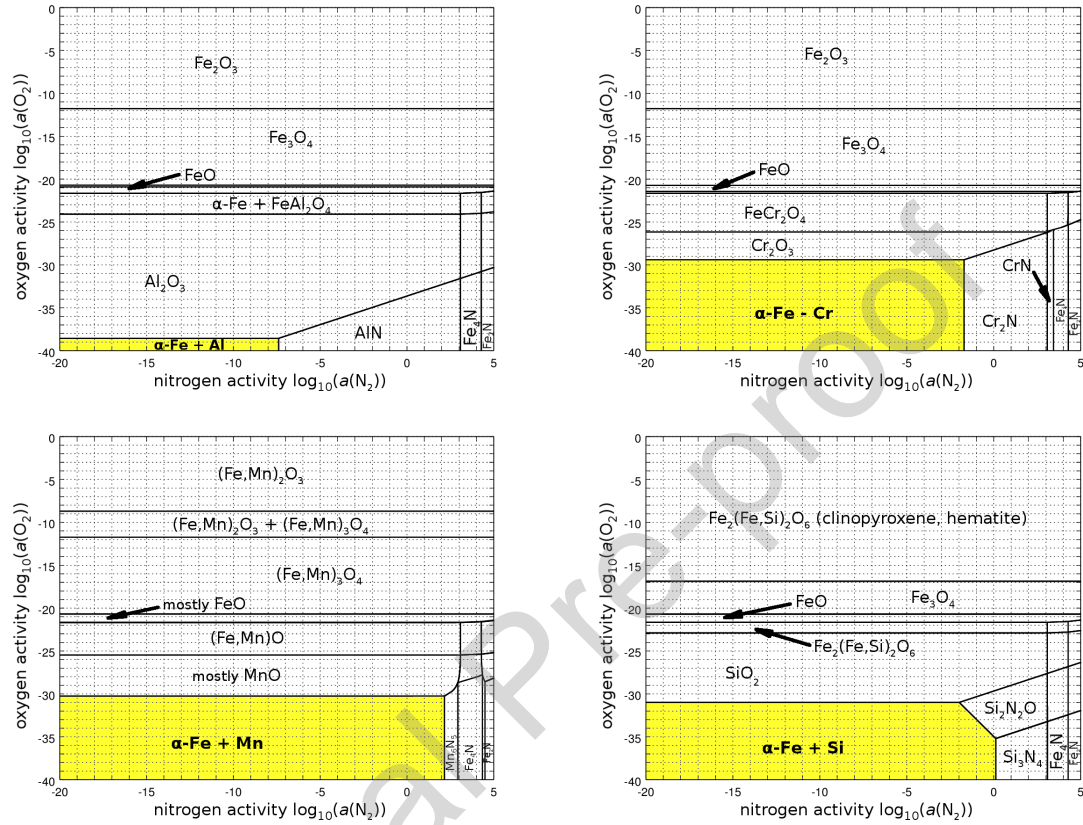
Appendix B. Predominance Diagrams

Figure B.8: Predominance diagrams of oxide vs. nitride stability in binary iron-based alloys containing Al, Cr, Mn and Si at 700 °C. The diagrams have been calculated with the FactSage Steels database (FSstel [48, 32]). Thermodynamic conditions where the pure metallic alloys without any oxides/nitrides are stable, have been highlighted in yellow.

13
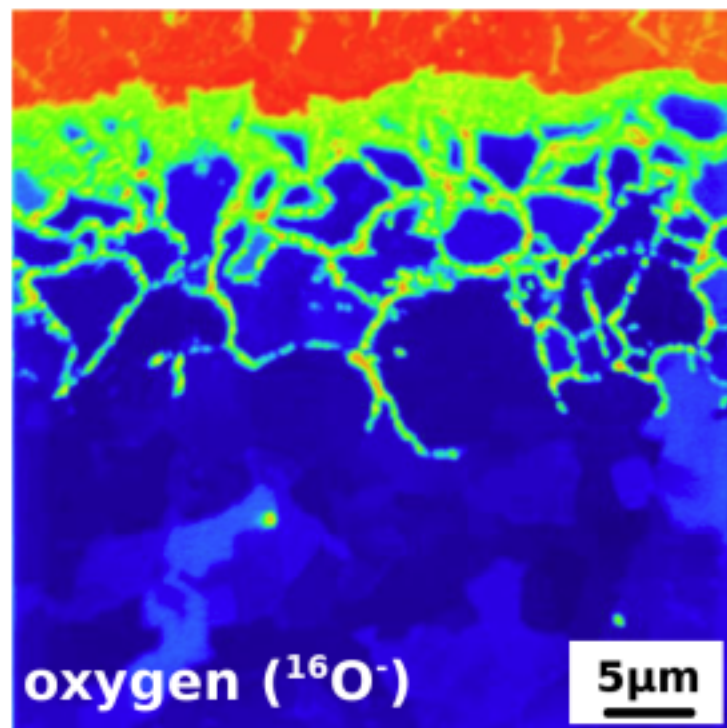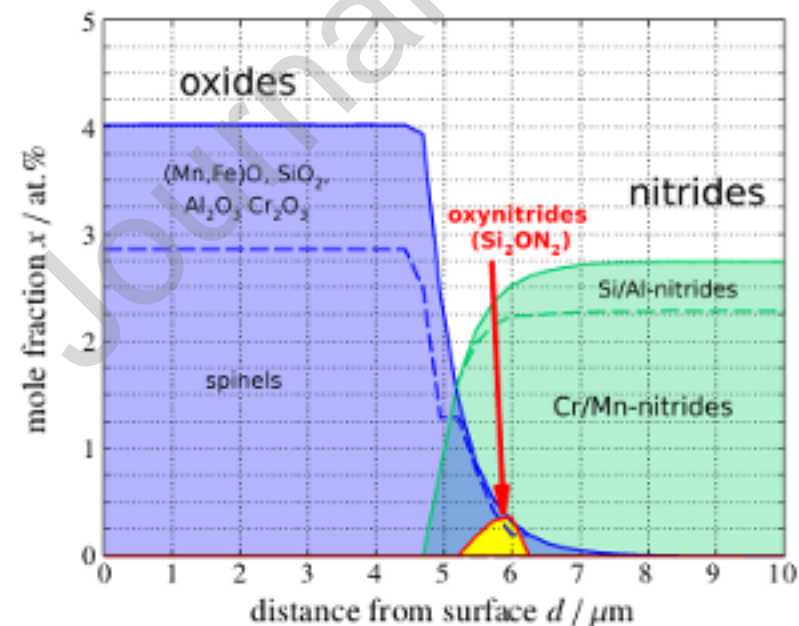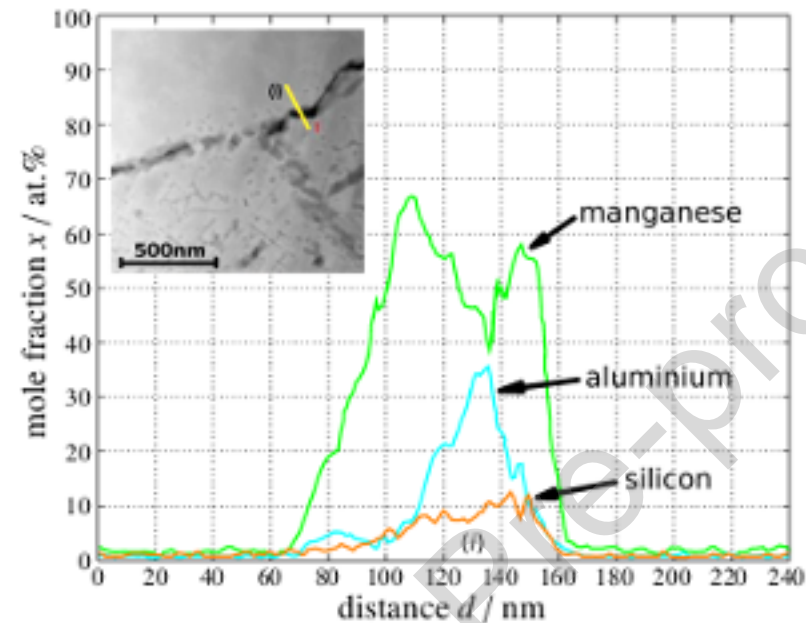
Credit Author Statement
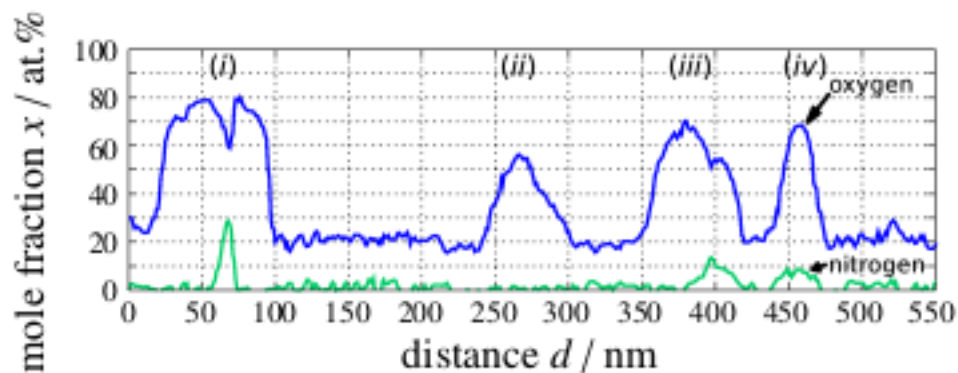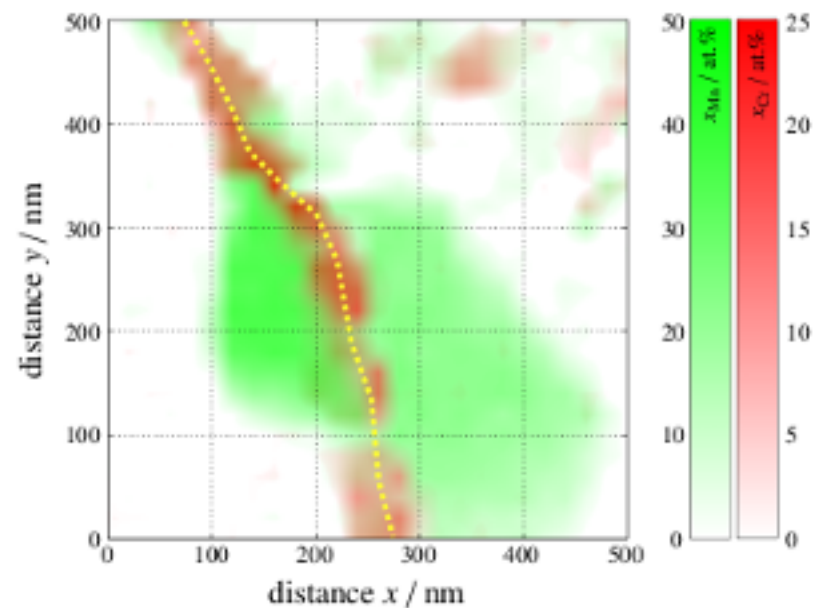
Vera G. Praig: sample preparation, experiments, discussions
Michael Stöger-Pollach: TEM/EELS measurements
Arno Schintlmeister: NanoSIMS measurements, discussions, publication writing, review
Michael Auinger: simulations, discussions, publication writing, review
Herbert Danninger: discussions, publication writing, review

Declaration of interests

☒ The authors declare that they have no known competing financial interests or personal relationships that could have appeared to influence the work reported in this paper.

☐The authors declare the following financial interests/personal relationships which may be considered as potential competing interests:

Highlights for Review

- high-resolution maps of grain boundaries show non-uniform element distribution

- Central nitride strand in oxides may originate from pre-existing nitrides

- Numerical calculations for >40 potentially stable phases are presented

- Differences between experiment and theoretical results will be discussed

- Existing knowledge on grain boundary oxide structure is strongly simplified